Carbon 175 (2021) 141–154

Contents lists available at ScienceDirect

Carbon

journal homepage: www.elsevier.com/locate/carbon

Research Article

Formation of one-dimensional quantum crystals of molecular deuterium inside carbon nanotubes

Carlos Cabrillo [a, *], Ricardo Fernández-Perea [a], Francisco Javier Bermejo [a], Leonor Chico [b], Claudia Mondelli [c], Miguel A. González [d], Eduardo Enciso [e], Ana M. Benito [f], Wolfgang K. Maser [f]

[a] Instituto de Estructura de la Materia, Consejo Superior de Investigaciones Científicas, Serrano 123, E-28006, Madrid, Spain
[b] Materials Science Factory, Instituto de Ciencia de Materiales de Madrid, Consejo Superior de Investigaciones Científicas, Sor Juana Inés de la Cruz 3, E-28049 Madrid, Spain
[c] Consiglio Nazionale delle Ricerche, Istituto Officina dei Materiali, Institut Laue Langevin, 71 avenue des Martyrs CS 20156, 38042, Grenoble Cedex 9, France
[d] Institut Laue Langevin, 71 avenue des Martyrs CS 20156, 38042, Grenoble Cedex 9, France
[e] Departamento de Química Física, Facultad de Ciencias Químicas, Universidad Complutense, Avenida Complutense s/n, E-28040, Madrid, Spain
[f] Instituto de Carboquímica, Consejo Superior de Investigaciones Científicas, Miguel Luesma Castán 4, E-50018, Zaragoza, Spain

ARTICLE INFO

Article history:
Received 28 October 2020
Received in revised form
10 December 2020
Accepted 23 December 2020
Available online 30 December 2020

Keywords:
Quantum solids
1D crystals
Confinement
Molecular hydrogen
Neutron scattering

ABSTRACT

Crystallization under stringent cylindrical confinement leads to novel quasi-one-dimensional materials. Substances with strong cohesive interactions can eventually preserve the symmetries of their bulk phase compatible with the restricted geometry, while those with weak cohesive interactions develop qualitatively different structures. Frozen molecular deuterium (D_2), a solid with a strong quantum character, is structurally held by weak dispersive forces. Here, the formation of one-dimensional D_2 crystals under carbon nanotube confinement is reported. In contradiction with its weak cohesive interactions, their structures, scrutinized using neutron scattering, correspond to definite cylindrical sections of the hexagonal close-packed bulk crystal. The results are rationalized on the grounds of numerical calculations, which point towards nuclear quantum delocalization as the physical mechanism responsible for the stabilization of such outstanding structures.

© 2020 Elsevier Ltd. All rights reserved.

1. Introduction

Carbon nanotubes are used to study crystallization under cylindrical constraints as well as to obtain a plethora of one-dimensional (1D) materials [1–3]. These new materials emerge, owing to the geometrical restriction, as crystalline phases with structures unlike their bulk counterparts (see chapter 5 in Ref. [3]). Some substances with strong cohesive interactions can retain their bulk crystallinity down to the strict one-dimensional limit, in which all the crystal constituents are simultaneously bulk and surface [4]. However, in general, for a certain level of geometrical restriction, crystalline arrangements with symmetries alien to the bulk phases develop [5]. As expected, this is the rule if the cohesive interactions are weak, for instance, hydrogen bonding in the archetypal case of water [6–8].

For purely dispersive interactions, molecular hydrogen (H_2) is an outstanding case owing to the strong quantum character of its condensed phases [9–11]. In particular, crystalline H_2 and its deuterium isotopologue (D_2) are prominent examples of quantum solids. Such crystals are characterized by a quantum nuclear delocalization sizable compared to the intermolecular distance, eventually rendering the harmonic crystal approximation useless [12]. The effect is maximized in the case of H_2, where quantum fluctuations are so dominant that make the crystal insensitive to thermal variations [10,11]. Furthermore, in both crystals the molecules behave as quantum free rotators, which implies that the nuclear orientational degrees of freedom are fully delocalized at low temperatures. Both crystalline states are van der Waals solids with an interaction potential well of just −2.77 meV, while that of the binding potential to a graphite surface amounts to $\simeq -50$ meV [13]. Confinement within narrow carbon nanotubes can roughly double this depth.

Calculations without including the quantum nuclear delocalization predict new ordered arrangements not present in the bulk [14–16], some of them reminiscent of spiral configurations

* Corresponding author.
E-mail address: ccabrilo@foton0.iem.csic.es (C. Cabrillo).

https://doi.org/10.1016/j.carbon.2020.12.067
0008-6223/© 2020 Elsevier Ltd. All rights reserved.

observed in the iodine 1D case [17–19]. The search for superfluid behavior has spurred intense theoretical efforts to deal with the quantum nature of the H_2 molecular movements [20–24]. The results, not free of controversy, seem to favor a quantum solid resembling neither the spiral arrangements nor the hexagonal close-packed (HCP) structure of the bulk phase [23]. In the case of molecular deuterium, nuclear wave function calculations hint at the possibility of HCP structures within narrow carbon nanotubes [25].

On the experimental side, as far as solidification under strong cylindrical confinement is concerned, the results are scarce. In carbon nanotubes, there is only evidence of transitions from one-to two-dimensional arrangements of D_2 on the external grooves of carbon nanotube bundles [26,27], but no results about crystal structures within the nanotubes. There are hints of HCP crystallization of D_2 in the cylindrical mesopores of silica-based MCM-41 materials [28], but with a pore diameter as wide as 2.5 nm, quite far from the 1D limit. In these studies D_2 is preferred because the strong incoherent neutron scattering of H_2 makes diffraction measurements impractical.

In this work, by resorting to neutron diffraction (ND), crystallization of molecular deuterium within multi-walled carbon nanotubes (MWCNT) is studied. We have succeeded in resolving the crystalline structure down to the strict 1D limit. In spite of the weakness of the cohesive interactions mentioned above, the 1D crystals preserve the structure of its bulk counterpart. The strong quantum character of the bulk crystalline D_2 is also preserved in the 1D confined phases: the large delocalization of the nuclear positions as well as the full quantum nature of the rotational degrees of freedom are manifest in the measured neutron diffraction. The structures of the discovered 1D crystals correspond to maximally symmetric cylindrical cuts of the bulk HCP crystal. Such structures were addressed after the failure in reproducing the measurements by fully atomistic molecular dynamics (MD) simulations as well as by dispersive density functional theory (DFT) calculations corresponding to our experimental conditions. Instead, DFT and MD approaches yield spiral-like arrangements in full agreement with energy considerations as well as consistent with previously reported calculations. Since such calculations do not deal with quantum nuclear effects, given the strong quantum nature of the observed structures we conclude that quantum delocalization in the nuclear degrees of freedom is essential to stabilize the discovered 1D crystals.

The paper is organized as follows: in section 2 the experimental procedures and setups are described. The results, in particular the finally resolved crystalline structures, are presented and discussed in section 3. In section 4 our findings are summarized and the main conclusions exposed. To lighten the exposition, the details of materials and methods as well as of the theoretical developments used in the data analysis are given as appendixes. Likewise, the large series of diffraction patterns explored along with a detailed description of the nonlinear fitting analysis used to resolve the structures are presented in a Supplementary Material file. For the sake of reproducibility, details of custom-made experimental setups and specifics of the numerical runs made are also given there. Finally, figures corresponding to some complementary measurements and tables of numerical parameters complete the Supplementary Material.

2. Experimental

Our main goal is to study the structural evolution of molecular deuterium during solidification under extreme cylindrical confinement. In short, we measured neutron diffraction (ND) in runs of 350 s while submitting a sample of open MWCNTs to thermal cycles (between 24.5 K and 2 K) at four increasing loads of adsorbed D_2 at 20 K, corresponding to the equilibrium pressures 62 hPa, 175 hPa, 225 hPa, and 284 hPa. The details of the experiment design, the experimental setup as well as of the materials and methods used are given in Appendix B.

We synthesized MWCNTs by the arc discharge method. Like in the single-walled case, the tubes in the raw material are closed. In order to open them, we submitted the samples to an oxidation treatment (for details, see Appendix B.2). Transmission electron microscopy (TEM) of the final material (see Fig. 1) shows the expected structure for typical arc discharge MWCNT samples: It is quite heterogeneous, showing a wide variety of MWCNTs among a plethora of irregular polyhedral closed nanostructures. The surfaces do not present eroded scars or holes other than the openings of some nanotubes.

The adsorption of the sample was characterized through an isothermal D_2 adsorption/desorption measurement at 20 K using a custom-made setup. The isotherm in Fig. 2 shows during desorption a hysteresis beginning at the bulk vapor pressure. This is expected in this kind of samples. It comes from macro/mesopores, i.e., the interstitials among the various structures observed in the TEM. Consistently with the opening of a portion of the MWCNTs, the isotherm also presents a small, but noticeable, almost vertical increase at zero pressure, a feature revealing the presence of micropores of molecular dimensions [29]. At sufficiently low loads of D_2, which correspond to low pressures in the isotherm, only the MWCNTs with the narrowest opened inner tubes are filled.

The chosen instrument was D20 at the Laue-Langevin Institute (ILL) in Grenoble, France, since it is a diffractometer of very high flux which allows to address very small quantities of scatterers in reasonable acquisition times (see details in Appendix B.6).

With respect to the neutron scattering, given the lightness of D_2 molecule, energy transfers between the incident neutron and the molecule affect the diffraction signal in a non-perturbative way. Usually this inelastic component is obtained heuristically since a proper correction requires a knowledge of the complete scattering law. Based on the neutron scattering theory for diatomic molecules developed by Sears [31], we have worked out an ansatz for the energy-integrated signal accounting for the observed $I_D(Q)$ (scattering from D_2 pairs; see section 3) that incorporates inelasticity without relying in any heuristic correction. From such an ansatz, the inelastic correction is given by a background, $bg(Q^2)$, expressible as an expansion in Q^2 (up to second order in practical terms). Physically, $I_D(Q)$ decomposes in a coherent and an incoherent part. The incoherent part stems from the random distribution of nuclear spin states along the sample. Formally is like the self-scattering contribution coming out from the scatterers. The coherent part of $I_D(Q)$ depends on the orientationally-averaged structure factor of the molecular center-of-mass (COM) specific arrangement of D_2 molecules. It can be calculated efficiently from the pair distribution function, i.e., the table of COM pair distances $d_{ij} = |\langle \mathbf{R}_i \rangle - \langle \mathbf{R}_j \rangle|$ and its associated multiplicities m_{ij}, where $\mathbf{R}_i$ is the position vector of the i molecule. An additional key ingredient to reproduce the ND coherent signal is a form factor corresponding to a spherical shell of diameter equal to the distance between the molecular nuclei, even in the solid phases at low temperature. This is a consequence of the nuclear orientational full delocalization. Likewise, the translational degrees of freedom also present a very significant quantum delocalization, which induces a large root mean square (rms) COM displacement. As explained in the next section, the observed diffraction signal reveals also the presence of oriented small crystals (or crystal) through barely discernible Bragg peaks. Although such precursor peaks can be ignored, we must consider the corresponding diffuse scattering, i.e., the diffraction signal between

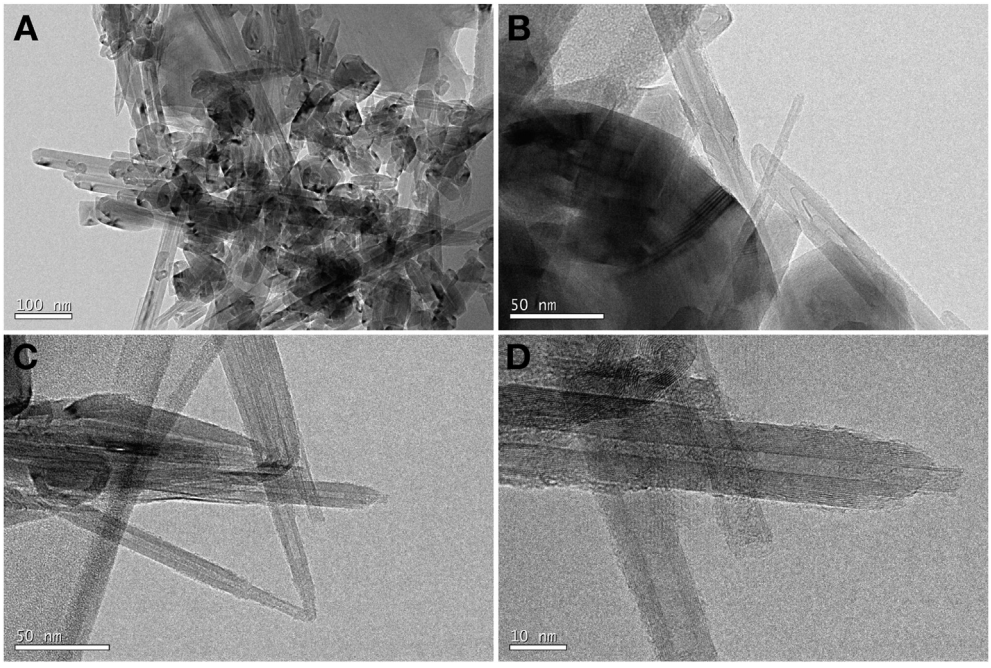

Fig. 1. Some TEM pictures of the final processed samples. A corresponds to X 30,000, B and C to X 100,000 and D to X 300,000.

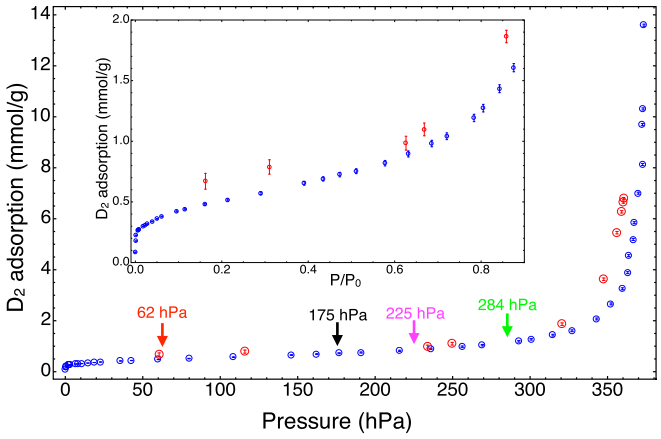

Fig. 2. D_2 adsorption (blue)/desorption (red) isotherm at 20.23±0.03 K for the sample of open MWCNTs. The amount of adsorbed gas is given in millimole per gram of sample. The arrows label the initial working points of the thermal cycles during the neutron diffraction measurements as described in the text. The inset is a zoom of the same data, focusing in the lower adsorption range in units of the bulk vapor pressure at 20.23 K (364.9 hPa [30]). (A colour version of this figure can be viewed online.)

Bragg peaks in a crystal, which arises from such oriented crystallites. This is well approximated by a term of the form $1-\exp(-Q^2u_{3D}^2/3)$ plus an incoherent part, where u_{3D} is the rms molecular displacement of the molecules belonging to such crystallite. There is also an instrumental background whose major contribution to $I_s(Q)$ is a flat noise accounted for in $bg(Q^2)$. With these basic constituents we have constructed a theoretical model of the expected ND as a function of the pair distribution functions of the confined structures with the corresponding rms COM displacement, the proportion of external crystallite scatterers, and its associated rms COM displacement. The detailed derivation is provided in Appendix A.1. The final expression for a concentration (mole fraction) C_{1D} of 1D confined molecules with a specific structure and a concentration C_{3D} of molecules in the 3D crystallite reads,

$$I_D(Q) = C_{1D}\left(4a_d^2 j_0(Qd_{D_2}/2)^2\left(S_{1D}^M(Q,u_{1D})-1\right)+F_{inc}(Q,u_{1D})\right) + C_{3D}\left(F_{inc}(Q,u_{3D}) - 4a_d^2 j_0(Qd_{D_2}/2)^2 \exp\left[-\frac{(Q\,u_{3D})^2}{3}\right]\right) + bg\left(Q^2\right), \quad (1)$$

where a_d is the neutron coherent scattering length of the deuteron, j_0 is the spherical Bessel function of zeroth order, d_{D_2} is the distance between the two deuterons, u_{1D} and u_{3D} are the corresponding rms molecular displacements, and the background reduces to $bg(Q^2) = bg_0 + bg_1\,Q^2 + bg_2\,Q^4$. $S_{1D}^M(Q,u_{1D})$ is the structure factor of the molecular COMs of the 1D crystal. The factor $j_0(Qd_{D_2}/2)^2$ is the spherical form factor mentioned above. The $F_{inc}(Q,u)$ terms are the incoherent part of the corresponding crystals. As explained in Appendix A.1, they depend not only in the temperature but in the concentration of ortho molecules. In practical terms our scattering intensity is not normalized to absolute units, so that C_{1D} and C_{3D} are scale factors proportional to the real concentrations.

With respect to the interference part $I_{DC}(Q)$ (scattering from D_2-C pairs; see section 3), by its very nature, it most prominent contribution is around 1.8 $Å^{-1}$ where the main MWCNTs Bragg peak is located, being negligible for larger values of Q since they correspond to spatial scales shorter than the D_2–C distances. This is confirmed a posteriori by the success of $I_D(Q)$ in reproducing the observed ND above 1.8 $Å^{-1}$. An atomistic description of $I_{DC}(Q)$ is exceedingly expensive in computational terms; instead, we have assumed the nanotubes as continuous and infinite to reduce the calculation to sums of analytical expressions as detailed in Appendix A.2. The approximated $I_{DC}(Q)$ depends on the inner radius of the cylinder where the confined phase forms, r_i, on the dispersion of the distribution of external MWCNTs diameters, σ_n, on the average interlayer distance within the MWCNTs, h, and on an effective rms displacement, u_{eff}, to take into the account the disorder in the involved pair distances. We remark that its intensity

with respect to $I_D(Q)$ is not free but determined by the calculation. Around 1.8 Å^{-1}, the $I_{DC}(Q)$ profile and its derivative change wildly in a few points, so that iterative minimization algorithms fail to converge. Instead, $I_{DC}(Q)$ is added as a correction to the fitted $I_D(Q)$, the corresponding free parameters chosen by visual inspection comparing series of plots of the modeled $I_s(Q)$ against the measurements. More specifically, u_{eff} is chosen to the minimum value that does not perturb the independently fitted $I_D(Q)$. The value of h essentially controls the position of the "dispersive" profile around 1.8 Å^{-1}. A value of 3.41 Å works well for all the explored cases. The inner radius, r_i, is the most relevant parameter with respect to the profile shape. As shown below our $I_{DC}(Q)$ reproduces qualitatively the "dispersive" profile around 1.8 Å^{-1}.

3. Results and discussion

Fig. 3 displays the ND signal $I(Q)$ as a function of the scattering vector modulus Q of the empty MWCNT sample (black) superimposed to that of the 284 hPa load (green) at low temperature. From now on and for the sake of simplicity, we label the loads by their equilibrium pressures at 20 K. The red rectangle encloses the four main observed Bragg peaks. The normalized area of $I(Q)$ within the rectangle during a thermal cycle for the two lower loads is shown in the inset. A reversible change of the slope appears at around 13.5 K in both cases, revealing a liquid/solid transition at that temperature. Given that the bulk triple point is at 18.73 K, and that we are under SVP conditions, such a temperature reduction indicates that the transition is happening under confinement [32]. Furthermore, since the transition temperature depends of the pore size, its reversibility implies confinement under a rather narrow distribution of pore sizes. On the contrary, the curves of the two larger loads show hysteresis, as expected from the heterogeneous distribution in size and shape of the interstitials observed in the TEM pictures at meso/macroscales (see Fig. S3 in the Supplementary Material for the hysteretic cases).

Fig. 4 displays the ND of the solid phases at the four loads after subtraction of the empty MWCNT signal, denoted as $I_s(Q)$. Here, solid phases refer to those below 11.5 K, a value chosen well under the 13.5 K where the liquid/solid transition manifests. Consistently, the ND of all the independent runs below 11.5 K do not show any discernible changes, so that all the runs with $T < 11.5$ K have been accumulated. Details of the neutron scattering data reduction are given in Appendix B.7. The 225 hPa and the 284 hPa loads present clear crystalline peaks identified as corresponding to both hexagonal close-packed (HCP) and face-centered cubic (FCC) phases. As shown in the figure, both kinds of peaks match to an excellent precision with strictly closed-packed arrangements with the same nearest-neighbor distance, namely, $d = 3.605$ Å, a value in agreement with those reported for the bulk solids [33,34]. The HCP phase is the fundamental crystal corresponding to the energy minimum of solid D_2, but FCC crystallization can also be observed as soon as any perturbation is introduced in the crystallization environment, as for example, the heterogeneous nature of our MWCNTs sample.

D_2 tends to crystallize in rather large crystal domains. Since the ND instrument relies on a horizontal narrow strip detector geometry (see Appendix B.6), the non-uniform distribution of crystal orientations leads to distorted peak heights and the extinction of peaks with decreasing D_2 load. At first glance the 175 hPa and 62 hPa patterns resemble those of amorphous substances with no Bragg peaks. A closer look, presented in the inset of Fig. 4, reveals the presence of a couple of precursors of bulk crystalline peaks at 175 hPa and one at 62 hPa. This can be appreciated better in Fig. 5. Since these Bragg peak precursors appear in both thermal cycles of 62 hPa and 175 hPa, they reveal oriented crystal growth somewhere in the sample-can system, probably owing to an inhomogeneity-related nucleation site. The "pseudo-amorphous" part necessarily corresponds to confined phases, in view of the behavior of the $I(Q)$ area of each load shown in the inset of Fig. 3. Within this respect, they depart significantly from the observed broader patterns in solid D_2 (10 K) adsorbed in SWCNT bundles [26]. There, the fits adscribe the ND to the presence of chains and stripes of D_2 molecules expected to be within the interstitials (chains) and external grooves (chains and stripes) of the bundles. These two loads are, therefore, the object of our main interest. The scattering from D_2 pairs, $I_D(Q)$, contributes dominantly to $I_s(Q)$. There is also a contribution from D_2 and carbon pairs, $I_{DC}(Q)$, relevant mainly below around 2 Å^{-1}. We focus first in modeling the dominant deuterium part, $I_D(Q)$.

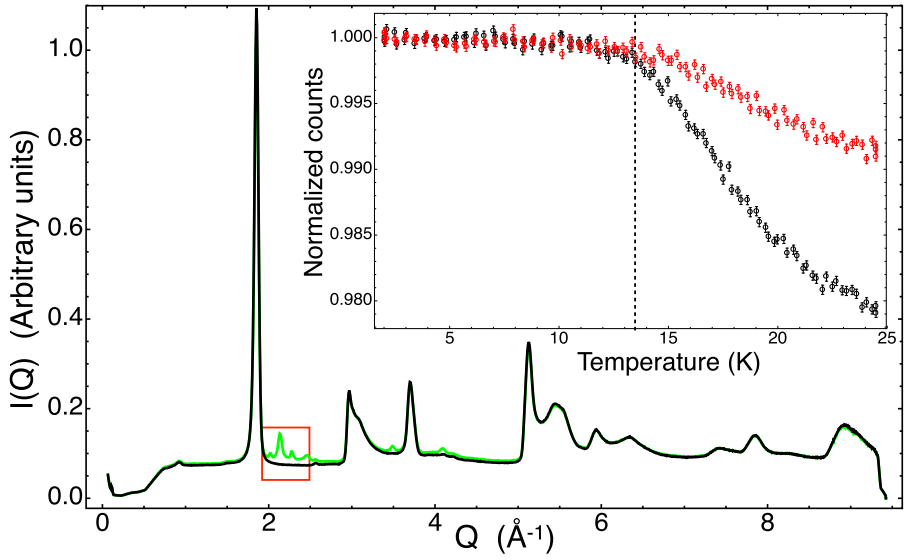

Fig. 3. Neutron diffraction pattern, $I(Q)$, from the pristine MWCNT sample (black) superimposed to that corresponding to the 284 hPa D_2 load (green) at low temperature. The inset shows the evolution during a thermal cycle of the area (normalized to one at 2 K) under $I(Q)$ within the red rectangle for the 62 hPa load (red circles) and for the 175 hPa case (black circles). (A colour version of this figure can be viewed online.)

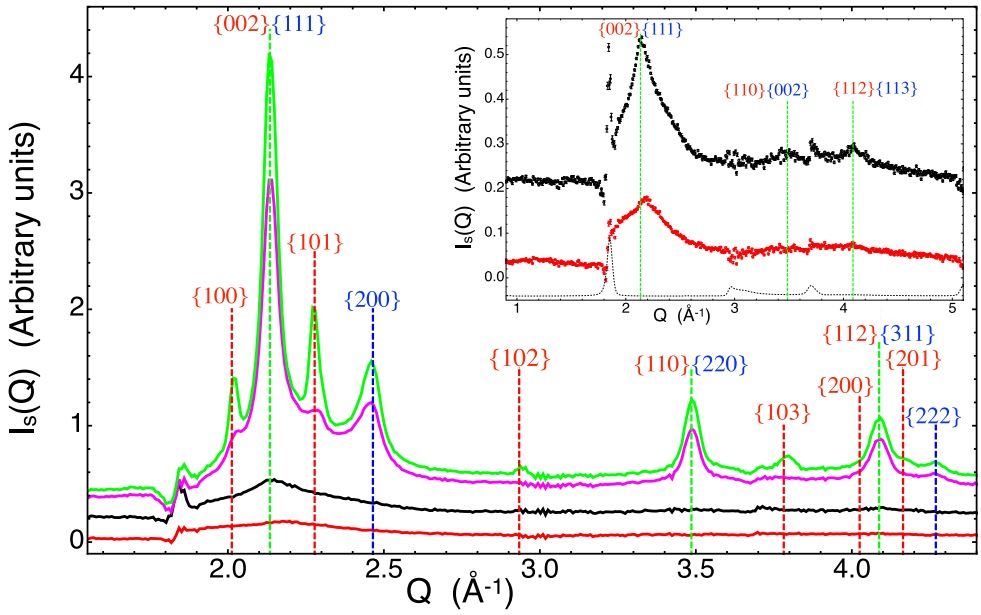

Fig. 4. $I(Q)$ after subtraction of the MWCNT sample contribution, $I_s(Q)$, for the 62 hPa (red), 175 hPa (black), 225 hPa (magenta), and 284 hPa (green) D_2 loads. The vertical dashed lines mark the position of the bulk solid D_2 crystalline peaks. Dashed blue lines are for peaks present only in the HCP crystal, red dashed lines for those only present in the FCC crystal and green dashed line for peaks belonging to both. On top of the dashed lines the corresponding Miller indexes are specified, in red for the HCP structure and in blue for the FCC case. The inset is a zoom of the two lowest loads, i.e., 62 hPa (red) and 175 hPa (black) along with a scaled-down version of the MWCNT sample $I(Q)$ (dotted line). (A colour version of this figure can be viewed online.)

Using the $I_D(Q)$ theoretical model described in section 2, a nonlinear fitting analysis detailed in the Supplementary Material was performed along a family of constrained nanostructures. We naturally started from structures obtained by MD simulations including MWCNTs up to five walls and effective potentials derived from state-of-the-art ab-initio calculations. Not surprisingly, they match the expected arrangements from energy minimization arguments: tubular shells adsorbed to the inner wall of the nanotubes that can be seen as rolled portions of the D_2 HCP crystal basal plane. As a matter of fact, they are explicit realizations of the tubular compact packing of spheres studied in the context of biological structures [35]. However, they are not compatible with our measurements as illustrated in Fig. S4, Supplementary Material.

Such disagreement drove us to consider other 1D crystalline structures corresponding to sections of maximal cylindrical symmetry of both the HCP and FCC bulk crystals with increasing diameter. For these crystals we fixed d to the value obtained from the 225 hPa and 284 hPa loads, i.e., 3.605 Å. Fig. 5 presents the final results of our nonlinear model fitting analysis. Let us consider first the 62 hPa load (Fig. 5A). The agreement is excellent just using a log-normal distribution in length (see inset) of the remarkable strict 1D crystal displayed in the right side of the figure. Differences of $I_D(Q)$ with increasing length become negligible (see Supplementary Material Figs. S10 and S11). Consequently, there is not enough information in the diffraction signal to discern the 1D crystal length distribution; in fact, a non-parametric fit of the crystal lengths only needs to populate a few isolated lengths to achieve excellent results. Lacking further information, we have relied in the log-normal distribution because it is usually observed in growth processes with preferential direction [36,37]. With respect to the ortho concentration, the fits need a proportion corresponding to room temperature, i.e., there was no para-ortho conversion during the experiment. The result is not only of a sheer beauty in its simplicity — the simplest nontrivial strict 1D compact crystal made out of spheres — but incompatible with theoretical predictions, as discussed above. It corresponds to a cylindrical cut of the minimal diameter which allows more than one molecule in the horizontal plane with the axis perpendicular to the hexagonal basal plane of the HCP fundamental bulk crystal, and centered so that it passes through the molecular centers at alternate layers. The six-fold symmetry of the parent HCP bulk crystal is reduced to three-fold (Fig. 5A, top right panel), so we call it triangular-close packed (TCP) 1D crystal.

Consistently, in the 175 hPa load (Fig. 5B) the nanocrystalline structure is just a radially enlarged version of the TCP 1D crystal. Again, there is a three-fold symmetry, as it can be seen in the transversal cut of the crystal, upper right panel of Fig. 5B. Since the crystal consists of alternating triangular and hexagonal layers, we denote it as THCP 1D crystal. Both 1D crystals display large rms COM displacements, around 0.33 Å in the TCP case, and 0.45 Å in the THCP counterpart, to be compared with the 0.46 Å obtained from neutron scattering of the D_2 bulk crystal [38] (see Tables SI and SII in Supplementary Material). Interestingly, there is no hint in the 175 hPa ND of the pattern corresponding to the 62 hPa load. Indeed, the fittings yield a zero population of the TCP phase, i.e., any finite population of the TCP phase worsens the fits. Should the TCP 1D crystals form also during the 175 hPa load in quantities comparable to the 62 hPa case, they would also manifest in the 175 hPa ND. Therefore, either the THCP crystals grew out of previously formed TCP seeds, or the MWCNTs of the smallest diameters are not filled during the 175 hPa load. In the first hypothesis, the TCP crystals grown at 62 hPa would be formed within MWCNTs of large enough inner diameter, whereas in the latter the two crystals would grow within MWCNTs of different inner diameters. Fortunately, the interference part, $I_{DC}(Q)$, carries information about the inner MWCNTs diameters so we can use it to settle this question. Fig. 5 shows in solid black the complete NDs including the $I_{DC}(Q)$ contribution. By construction, it coincides with $I_D(Q)$ above ~ 1.8 Å^{-1} so that it falls below the red line representing $I_D(Q)$. As shown in the top right panels of Fig. 5, the chosen inner diameters $2r_i$ (10.53 Å for the TCP and 14.09 Å for the THCP) accommodate well the D_2 molecules in terms of the estimated locus [39] of the

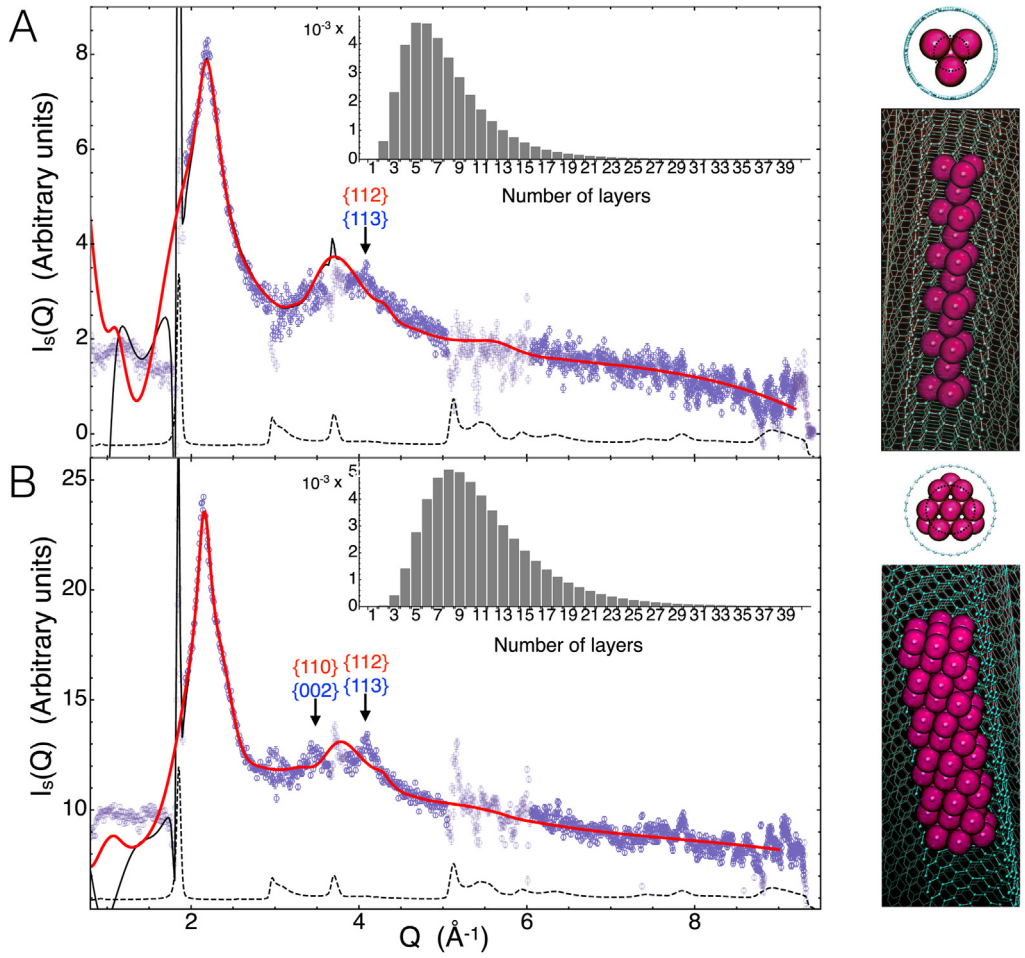

Fig. 5. D_2 1D crystals fitting the ND data. (A) D_2 load corresponding to the 62 hPa case. (B) D_2 load corresponding to the 175 hPa case. ND data points displayed in light blue are not included in the fittings (points below 2 Å^{-1}, areas too affected by MWCNT peak subtraction, and some outliers). Solid red curves are the fitted $I_D(Q)$ component. Thin black curves show the final $I_s(Q)$ including the $I_{DC}(Q)$ part. The dashed lines are a down-scaled representation of the pristine MWCNT sample ND. Arrows mark the positions of some relevant Bragg peaks of the bulk crystal. At the right side, a representative structure giving rise to the corresponding $I_s(Q)$ is shown in perspective. The small spheres have a diameter equal to the deuteron-deuteron distance of the D_2 molecule (0.74 Å). The diameter of the semitransparent larger spheres equals $d = 3.605$ Å. In the top views only the inner nanotubes are shown, an (11,4) single-walled CNT (A) and an (18,0) (B). Dotted circumferences mark the position of the minimum of the adsorption potential. Insets display the fitted log-normal distributions of 1D crystal lengths in terms of the number of molecular layers perpendicular to the MWCNT axis. (A colour version of this figure can be viewed online.)

adsorption potential minima. However, inner diameters around 14 Å in the TCP case render $I_{DC}(Q)$ profiles incompatible with the measured ND at 62 hPa. We are therefore left to conclude that the MWCNTs of the narrowest inner diameters are not significantly filled during the 175 hPa load. Since we are referring to pore sizes at the molecular limit (below two molecular diameters), steric molecular hindrance as well as anomalous capillary and condensation effects [40–42], dependent on the D_2 load, seem plausible. Within this respect, the irregular shapes and the functional groups at the entrance of the opened nanotubes could play a relevant role. For instance, funnel-like attractive potentials at the entrance would probably enhance the possibility of molecular jamming at 175 hPa owing to the different kinetics and density with respect to the 62 hPa case. Given the large de Broglie wavelength of D_2, quantum wave-like behavior contributing to these effects, as observed with He [43–45], are also conceivable. At any rate, here we can only speculate about the microscopic mechanisms involved in this interesting anomalous behavior since their elucidation requires a study by its own.

Taking into the account that MD simulations do not describe accurately dispersive interactions, which are crucial in this kind of systems, we have performed advanced dispersive DFT calculations validated against experiments, in order to shed light on the discrepancy between the observed structures and theoretical predictions (details of the calculations are given in Appendix B.9 and Supplementary Material). Due to the large computational demand of this approach, we restrict ourselves to SWCNTs of a diameter compatible with the TCP 1D crystal. More specifically, the nanotube of chiral vector (10,5) has an adequate unit cell length while its diameter of 10.36 Å is just 2% below that of the (11,4) tube shown in Fig. 5A. The number of D_2 molecules is chosen to be eleven, corresponding to five layers of the 1D TCP crystal, the most probable length (inset of Fig. 5A). Fig. 6 summarizes the DFT results. Spiral geometries similar to those obtained by MD are once more the most stable configurations, at variance with the experimental results (see Fig. S4A of Supplementary Material). Remarkably, the observed 1D TCP structure, presented in Fig. 6B, is metastable within this approach, but the next most plausible 1D crystal derived from the FCC bulk structure is not stable under the DFT approximation (depicted in Fig. S4B of Supplementary Material). The calculated $I_D(Q)$s are also shown in Fig. 6 along with those corresponding to the equivalent TCP 1D structure obtained from the fits. Additionally, notice that the DFT calculations yield an effective nearest-neighbor distance slightly shorter than the experimental one. This is a

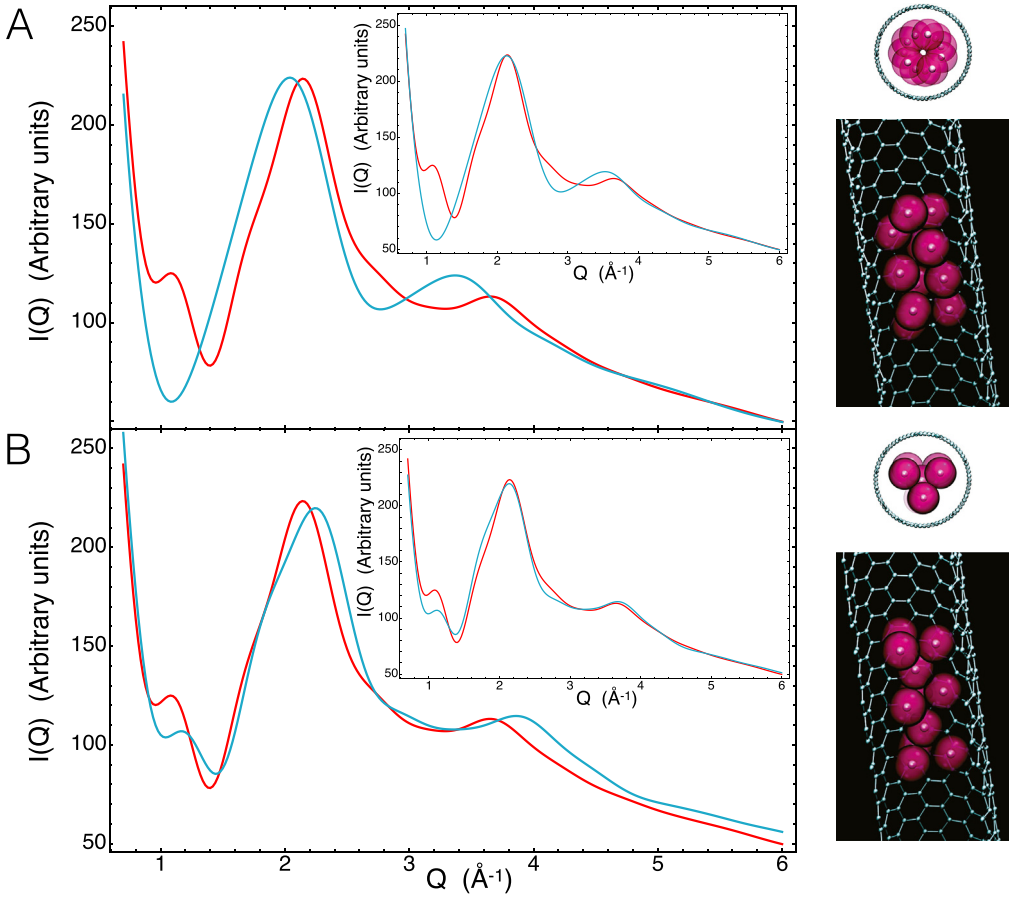

Fig. 6. 1D structures obtained by dispersive DFT calculations. (A) Fundamental structure corresponding to the lowest energy minimum. (B) Structure of the 1D TCP kind corresponding to a metastable energy minimum. Their associated $I_D(Q)$s are also shown (cyan curves) along with that corresponding to the experimentally-determined equivalent 1D TCP crystal (red curves). Since the DFT calculations do not reproduce the nearest-neighbor distance accurately, properly Q-rescaled versions of the $I_D(Q)$s are displayed in the insets. (A colour version of this figure can be viewed online.)

consequence of the quantum delocalization of the rotational degrees of freedom of the nuclei, not taken into account by the DFT approach, which renders the molecular interactions essentially isotropic. On the contrary, within the DFT approximation the D_2 molecules retain its dumbbell-like anisotropic character and tend to order in a parallel, more compact, configuration.

The present results tell of a van der Waals molecular compound that crystallizes retaining the bulk crystal structure down to the strict 1D limit. This is in stark contrast with results pertaining to other materials with weak cohesive energies, which do not show the marked quantum behavior in their translational and/or rotational degrees of freedom as our 1D crystals do, conspicuously revealed by their neutron scattering response. Our DFT calculations, with reliable dispersive functionals, make clear that the missing quantum treatment of the nuclear motions are one key ingredient for the stabilization of these 1D crystals. On the other hand, the fact that the TCP 1D crystal is weakly metastable under the DFT calculations suggest that a precise account of the quantum behavior of the electronic cloud in the description of the dispersive interactions could also be relevant. In fact, the development of dispersive DFT techniques during the last two decades is characteristic of the nanoscience revolution: adsorption phenomena within nanostructures depend too subtly on the dispersive interactions to be accommodated within the traditional effective potential approach. The challenge now is to incorporate the nuclear quantum effects accurately, a subject attracting an increasing interest [46]. At present, inclusion of translational quantum nuclear delocalization effects in condensed matter can be tackled with computationally very demanding quantum Monte Carlo or path integral methods [23,24] but we remark that, both, the nuclear rotational delocalization and the dispersive forces are treated in the same effective manner as in our MD simulations. Within this context, the structures here discovered stand out for testing future theoretical developments since they are dispersive molecular solids displaying a non-trivial quantum nuclear behavior at the same time being structurally simple.

4. Conclusion

Using neutron diffraction we have discovered 1D quantum crystals of molecular deuterium within MWCNTs. Unexpectedly for a molecular solid with very weak cohesive interactions, the 1D crystals preserve the structure of the HCP bulk D_2 crystal. Neither atomistic molecular dynamics simulations nor advanced dispersive DFT calculations predicts such a possibility, signaling the strong quantum nuclear effects as essential to the emergence of the discovered 1D crystals.

These 1D crystals are the simplest nontrivial condensed matter systems in which the quantum nature, not only of the electronic cloud, but also of the nuclear translational and rotational degrees of freedom, plays an essential role. Our results are deemed to be of special relevance, since they provide a testbed to confront theoretical approaches aimed to understand and incorporate accurately the full quantum nature of real interactions, including the nuclear

degrees of freedom. Such advances will have a bearing on the design and simulation of novel (possibly quantum) materials.

CRediT authorship contribution statement

Carlos Cabrillo: Conceptualization, Methodology, Software, Formal analysis, Investigation, Writing - original draft, Visualization, Supervision, Project administration, Funding acquisition. **Ricardo Fernández-Perea:** Conceptualization, Software, Investigation, Writing - review & editing, Visualization. **Francisco Javier Bermejo:** Conceptualization, Writing - review & editing, Project administration, Funding acquisition. **Leonor Chico:** Conceptualization, Investigation, Writing - original draft. **Claudia Mondelli:** Conceptualization, Formal analysis, Methodology, Investigation, Resources, Writing - review & editing. **Miguel A. González:** Conceptualization, Formal analysis, Investigation, Resources, Writing - review & editing. **Eduardo Enciso:** Conceptualization, Investigation, Writing - review & editing, Project administration, Funding acquisition. **Ana M. Benito:** Conceptualization, Investigation, Resources, Writing - review & editing. **Wolfgang K. Maser:** Conceptualization, Investigation, Resources, Writing - review & editing, Project administration, Funding acquisition.

Declaration of competing interest

The authors declare that they have no known competing financial interests or personal relationships that could have appeared to influence the work reported in this paper.

Acknowledgements

This work has been partly supported by the Spanish Agencia Estatal de Investigación (AEI), Fondo Europeo de Desarrollo Regional (FEDER, EU), Ministerio de Economía y Competitividad (MINECO), Ministerio de Ciencia, Innovación y Universidades (MCIU), under Grants No. MAT2016-75354-P (AEI/FEDER, EU), FIS2015-64654-P (MINECO/FEDER, EU), MAT2015-68394-R (MINECO/FEDER, EU), PGC2018-097018-B-I00 (MCIU/AEI/FEDER, EU), MAT2012-33633 (MINECO/FEDER, EU), MAT2012-39199-C02-02 (MINECO/FEDER, EU), by EU COST Action CM1405 “Molecules in Motion” (MOLIM), and by Spanish Ministerio de Ciencia e Innovación under Grants No. MAT2007-65711-C04-01, MAT2007-65711-C04-05, MAT2002-04540-C05-02, MAT2002-04540-C05-03, and MAT2002-04540-C05-04. We thank Thomas Hansen for his assistance during the neutron diffraction experiments, and Francesco Albergamo for kindly offering us the volumetric setup for the D_2 adsorption measurements. We thank also the ILL sample environment group, and, in particular, J. P. Gonzales, for the superb support during the preparation and realization of the neutron diffraction and D_2 adsorption experiments. Finally, we thank the Super Computer Center of Galicia (CESGA) for the provided computational resources.

Appendix C. Supplementary data

Supplementary data to this article can be found online at https://doi.org/10.1016/j.carbon.2020.12.067.

Appendix A. Theoretical developments

Appendix A.1 Theory of the measured neutron scattering

In a neutron diffraction experiment at a continuous source installation such as the ILL, the intensity of scattered neutrons by the sample out of a mono-energetic incident neutron beam is measured as a function of the scattering angle. The relevant differential scattering cross section is then given by

$$\frac{d\sigma}{d\Omega} = \int_{-\infty}^{E_i} \frac{d^2\sigma}{d\Omega\, dE_f}\, dE_f \,, \tag{A.1}$$

where the Ω denotes solid angle, E_i the energy of the incident neutrons and E_f the final detected neutron energy. Following the full quantum calculations of Sears [31], the double differential cross section in the case of a homonuclear diatomic molecule under the assumption of free rotation, can be expressed as

$$\frac{d^2\sigma}{d\Omega\, dE_f} = N\frac{k_f}{k_i}\Big(4\, a_d^2\, j_0(Qd_{D_2}/2)^2 S_{int}(\mathbf{Q},E) + \sum_{J,J'} a^2(Q;J,J') S_{self}(Q,E-E_{J,J'})\Big). \tag{A.2}$$

Here N is the number of nuclei in the sample, $k_{i,f}$ are the initial and final neutron angular wavenumbers, a_d is the coherent neutron scattering length of the deuteron, j_0 the spherical Bessel function of zero order, d_{D_2} the distance between the nuclei in the molecule, $\mathbf{Q}$ is the scattering angular wavevector (Q its norm), the Js denote the nuclear orbital angular momentum quantum levels, $E_{J,J'}$ the corresponding energy jumps among J levels and $E = E_i - E_f$ is the energy transfer. The $a^2(Q;J,J')$ factors are quite complex expressions involving linear combinations of Bessel spherical functions dependent on the bosonic or fermionic character of the nuclei [31]. They depend on all the rotational levels excited by the neutrons at the given incident energy and, as such, incorporate the corresponding orientational form factors. Transitions between the ortho (even J angular momentum) and para (J odd) levels are forbidden so that thermalization of the populations proceeds independently. The $J = 1$ state is highly metastable so that equilibration at low temperatures downwards the fundamental $J = 0$ level is extremely slow in the bulk [12] but it could be accelerated by the interaction with the substrate. Otherwise, thermal equilibration proceeds unhindered so that the model depends on the temperature and the concentration of ortho molecules [31].

$S_{int}(\mathbf{Q},E)$ is the interference part of the dynamical structure factor of the molecular COMs, i.e., the part not involving single particle self-scattering. Such self-scattering part (of the COMs) corresponds to $S_{self}(Q,E)$ (Sears uses the subscript *inc* from incoherent). It is a consequence of the free rotation assumption that both $S_{int}(\mathbf{Q},E)$ and $S_{inc}(Q,E)$ in Eq. (A.2), refer only to the dynamics of the COMs of the molecules. In order to calculate Eq. (A.1), we need a model of such dynamical structure factors. Since their contribution to Eq. (A.1) is through integration in E, we will take advantage of general sum rules, i.e., moments in E, that must be satisfied independently of the system dynamics.

Focusing on the interference part, the relevant sum rule is $\int_{-\infty}^{\infty} S_{int}(\mathbf{Q},E)\, dE = S(\mathbf{Q}) - 1$, where the $S(\mathbf{Q})$ is the structure factor. This is the quantity of interest, since it yields a structural characterization of the system and it is amenable to theoretical modeling. It is given by

$$S(\mathbf{Q}) = 1 + \frac{1}{N}\sum_{i\neq j}\langle \exp[i(\mathbf{R}_i - \mathbf{R}_j)\cdot\mathbf{Q}]\rangle \,, \tag{A.3}$$

where N is the number of scatterers, $\mathbf{R}_j$ the position vector of the j molecular COM and $\langle\rangle$ denotes quantum-mechanical thermal average. In a solid, thermal fluctuations are well approximated by a Gaussian distribution of displacements around the mean positions

$\langle \mathbf{R}_j \rangle$. In such a case, after orientational and thermal average, Eq. (A.3) reduces to

$$S(Q) = 1 + \frac{1}{N}\sum_{i\neq j} j_0\left(\left|\langle \mathbf{R}_i\rangle - \langle \mathbf{R}_j\rangle\right| Q\right)\, e^{-\frac{1}{3}u^2\, Q^2} = 1 + \frac{1}{N}\sum_{d_{ij}} m_{ij}\, j_0(d_{ij}Q)\, e^{-\frac{1}{3}u^2\, Q^2}\,, \tag{A.4}$$

where the final sum is over all the different pair distances $d_{ij} = \left|\langle \mathbf{R}_i\rangle - \langle \mathbf{R}_j\rangle\right|$, m_{ij} are the corresponding multiplicities and u is the rms displacement around the $\langle \mathbf{R}_j\rangle$, assumed here, isotropic and independent of the position. In a solid, the vast majority of the interference scattering is elastic, i.e., it accumulates around $E = 0$, so that our model for the interference part is $S_{int}(Q,E) = (S(Q) - 1)\,\delta(E)$, where $\delta(E)$ denotes the Dirac delta.

With respect to the self part the elastic term amounts to

$$S^{e}_{self}(Q,E) = e^{-\frac{1}{3}u^2\, Q^2}\,\delta(E)\,. \tag{A.5}$$

However, it is not so dominant as in the interference case, so we need to proceed further. The relevant moments to develop a model of the inelastic part are [47].

$$\int_{-\infty}^{\infty} S_{self}(Q,E)\, dE = 1\,, \tag{A.6}$$

$$\int_{-\infty}^{\infty} E\, S_{self}(Q,E)\, dE = \frac{\hbar^2 Q^2}{2M} = E_r\,, \tag{A.7}$$

$$\int_{-\infty}^{\infty} E^2\, S_{self}(Q,E)\, dE = \frac{4}{3}E_r\overline{K} + E_r^2\,, \tag{A.8}$$

where M is the mass of the molecule, E_r is the so-called recoil energy and $\overline{K}$ is the mean kinetic energy. The zeroth order moment is always satisfied, the first order moment is satisfied provided that the interaction does not depend on the molecular velocities, and the second is true for isotropic systems. The elastic part does not contribute to the first and second moment; decomposing the incoherent part as $S_{self}(Q,E) = S^{e}_{self}(Q,E) + S^{ine}_{self}(Q,E)$ and using Eq. (A.5), the zeroth moment implies

$$\int_{-\infty}^{\infty} S^{ine}_{self}(Q,E)\, dE = 1 - e^{-\frac{1}{3}u^2\, Q^2}\,. \tag{A.9}$$

On the other hand, from the first and the second moments, the energy dispersion is obtained:

$$\sigma_E^2 = \langle E^2\rangle - \langle E\rangle^2 = \frac{4}{3}E_r\overline{K}\,. \tag{A.10}$$

The mean kinetic energy at low temperature is expressed in terms of the rms displacement as [48,49],

$$\overline{K} = \frac{9}{16}\Theta = \frac{81}{64}\frac{\hbar^2}{Mu^2}\,, \tag{A.11}$$

where Θ is the Debye temperature, the parameter usually quoted in the experimental reports. We are now in disposition to write up a model for the incoherent part preserving all the moments up to the second:

$$S^{M}_{self}(Q,E) = e^{-\frac{1}{3}u^2\, Q^2}\,\delta(E) + \left(1 - e^{-\frac{1}{3}u^2\, Q^2}\right)\frac{1}{\sqrt{2\pi\sigma_E^2}} \exp\left[-\frac{(E-E_r)^2}{2\sigma_E^2}\right]. \tag{A.12}$$

where the M superscript serves to recall it refers only to molecular COM contribution. The chosen Gaussian shape for the inelastic scattering is a natural choice to warrant the integral properties up to second order. Such a profile must be understood as a kind of smoothing of the real signal since it does not incorporate the details of the density of vibrational modes. Only in the limit of very large momentum transfer the same kind of profile would be exact (impulse approximation) but for the nuclei themselves, not for the molecular COMs. Interestingly, in the case of H_2, given the lightness of the molecule, this profile for the COM dynamics has been observed at least from Q's as low as 5 Å^{-1} [50].

In order to calculate Eq. (A.1) the factor $k_f/k_i = k_i\sqrt{1 - E/E_i}$ must be also included in the inelastic part. Conservation of energy and momentum establishes a relation among Q, E, and, φ, the angle between $\mathbf{k_i}$ and $\mathbf{k_f}$, namely,

$$Q^2 = k_i^2 + k_i^2\left(1 - \frac{E}{E_i}\right) - 2k_i^2\sqrt{1 - \frac{E}{E_i}}\cos\varphi\,. \tag{A.13}$$

Substituting Q in terms of E and φ, the integration of Eq. (A.2) in E yields the measured cross section Eq. (A.1). Notice that direct integration of Eq. (A.2) does not yield the single cross section, since it is defined (and measured) at constant φ, not at constant Q. However, usually the ND is expressed in terms of Q, but only at its elastic value using the relation $Q_e = 2k_i\sin\varphi/2$. As a rule, the elastic condition is not explicitly stated but the same symbol Q is used. We adhere here to such a practice. At any rate, in many experiments E_i is sufficiently high for the static approximation to be valid [47], where all the scattering can be considered elastic.

As far as the fitting is concerned, we first generate a two-dimensional numerical table in u and Q of the expression

$$F_{inc}(Q,u) = \int_0^{\infty}\frac{k_f}{k_i}\sum_{J,J'} a^2(Q;J,J')S_{self}\left(Q, E - E_{J,J'}\right)\, dE\,, \tag{A.14}$$

where the suffix *inc* remarks that this expression includes not only the coherent self-contribution but the incoherent scattering. In the actual fittings a two-dimensional interpolation of the table is used to avoid the computational load of a numerical integration at each fitting step.

With respect to the diffuse coherent scattering of the external crystallite, performing only the thermal average in Eq. (A.3), we have

$$\begin{aligned} S(\mathbf{Q}) &= 1 + \frac{e^{-\frac{1}{3}u^2\, Q^2}}{N}\sum_{i\neq j} e^{i\left(\langle \mathbf{R}_i\rangle - \langle \mathbf{R}_j\rangle\right)\cdot\mathbf{Q}} \\ &= 1 + e^{-\frac{1}{3}u^2\, Q^2}\left(\frac{1}{N}\sum_i\left|e^{i\langle \mathbf{R}_i\rangle\cdot\mathbf{Q}}\right|^2 - 1\right) \\ &= 1 - e^{-\frac{1}{3}u^2\, Q^2} + e^{-\frac{1}{3}u^2\, Q^2}\,\frac{1}{N}\sum_i\left|e^{i\langle \mathbf{R}_i\rangle\cdot\mathbf{Q}}\right|^2 \\ &= 1 - e^{-\frac{1}{3}u^2\, Q^2} + S_B(\mathbf{Q})\,. \end{aligned} \tag{A.15}$$

In a crystal, and in the limit of $N\to\infty$, $S_B(\mathbf{Q})$ gives rise to the Dirac delta peaks characteristic of Bragg scattering. The rest is

obviously the scattering among the Bragg peaks, i.e., the diffuse scattering. This remains true also at finite N, where the peaks broaden. Therefore, the diffuse scattering from external crystallite contributes with an interference part given by

$$S_{int}(\mathbf{Q},E) = -e^{-\frac{1}{3}u^2\,Q^2}\delta(E)\,, \tag{A.16}$$

while the incoherent part is again given by $F_{inc}(Q,u)$, but this time with u corresponding to that of the external crystallite.

Altogether, for a number concentration C_{1D} of 1D confined molecules and a C_{3D} number concentration of molecules in the 3D external small crystal, gives,

$$I_D(Q) = C_{1D}\left(4a_{coh}^2\, j_0(Qd_{D_2}/2)^2\left(S_{1D}^M(Q,u_{1D})-1\right)+F_{inc}(Q,u_{1D})\right) + C_{3D}\left(F_{inc}(Q,u_{3D}) - 4a_{coh}^2\, j_0(Qd_{D_2}/2)^2 \exp\left[-\frac{(Q\,u_{3D})^2}{3}\right]\right), \tag{A.17}$$

where $S_{1D}^M(Q,u_{1D})$ is the structure factor of the molecular COMs as given by Eq. (A.4) and u_{1D} and u_{3D} are the corresponding rms displacements.

Besides Eq. (A.18) there must be an instrumental flat background, bg_0. With such an addition, Eq. (A.18) produces convergent fits to the measured $I(Q)$. That is, it captures adequately most of the ND signal. A final refinement is now expressible as series in Q^2. A background second order in Q^2, $bg_0 + bg_1Q^2 + bg_2Q^4$, is enough to obtain excellent fits.

Appendix A.2 Modeling of the $D_2 - C$ diffraction interference term

In terms of the positions of the D_2 COMs, $\mathbf{R}_i$ and of the carbon atoms, r_j, the ND signal corresponding to the interference between carbon atoms and D_2 molecules reads,

$$I_{DC}(Q) = C_{1D}\, a_c\, 2\, a_d\, j_0(Qd_{D_2})\frac{1}{N}\sum_i\sum_j \langle e^{-i\mathbf{Q}\cdot(\mathbf{R}_i-\mathbf{r}_j)}\rangle + c.c.$$

$$= C_{1D}\, a_c\, 2\, a_d\, j_0(Qd_{D_2})\, e^{-\frac{1}{6}Q^2\left(u_{1D}^2+u_c^2\right)}\frac{1}{N}\sum_i\sum_j \langle e^{-i\mathbf{Q}\cdot(\langle\mathbf{R}_i\rangle-\langle\mathbf{r}_j\rangle)}\rangle + c.c.\,, \tag{A.18}$$

where $c.c.$ denotes complex conjugate, N is the number of molecules, a_c is the coherent neutron scattering length of carbon nuclei, u_c their rms mean displacement and in the second equality we have performed thermal average, again assumed Gaussian and isotropic. Consequently, $\langle\rangle$ reduces to only an orientational average. Here, $2\,a_d\,j_0(Qd_{D_2})$ plays the role of the coherent scattering length of the D_2 molecule, dependent on Q owing to the non point-like molecular structure.

An atomistic description of the MWCNTs is computationally too expensive. However, assuming a continuous distribution of the carbon atoms along infinite tubes, we can take advantage of some analytical calculations. Given a microscopic density of carbon atoms, $\rho_c(\mathbf{r})$, a general term of the sums above is written as

$$\langle e^{-i\mathbf{Q}\cdot\langle\mathbf{R}_i\rangle}\int_V e^{-i\mathbf{Q}\cdot\mathbf{r}}\rho_c(\mathbf{r})\,d\mathbf{r}^3\rangle = \frac{1}{4\pi}\int d\Omega_Q\, e^{-i\mathbf{Q}\cdot\langle\mathbf{R}_i\rangle}\int e^{i\mathbf{Q}\cdot\mathbf{r}}\rho_c(\mathbf{r})\,d\mathbf{r}^3\,, \tag{A.19}$$

where $d\Omega_Q$ is the solid angle corresponding to a direction of the scattering vector and the integrals extend to all the directions and the whole space respectively. For an infinite tube of diameter R_{CNT}, the density is expressed in the cylindrical coordinates r,ϕ,z, with z axis that of the cylinder as $\rho_c(\mathbf{r}) = \rho_A\delta(r-R_{CNT})$, being ρ_A the areal density of carbon in the nanotube. Analytical integration in the cylindrical coordinates yields

$$\int e^{i\mathbf{Q}\cdot\mathbf{r}}\rho_c(\mathbf{r})\,d\mathbf{r}^3 = 4\pi^2\rho_A\,R_{CNT}\,J_0(QR_{CNT})\,\delta(Q_z)\,, \tag{A.20}$$

where J_0 is the Bessel function of order zero and Q_z is the z component of the scattering vector. Notice that for an infinite tube the symmetry leads to cancellation of the dependence along the z axis. Substituting Eq. (A.21) in Eq. (A.20), again analytical integration can be done, this time using spherical coordinates, so that

$$\langle e^{-i\mathbf{Q}\cdot\langle\mathbf{R}_i\rangle}\int_V e^{-i\mathbf{Q}\cdot\mathbf{r}}\rho_c(\mathbf{r})\,d\mathbf{r}^3\rangle = 2\pi^2\rho_A\,R_{CNT}\,J_0(QR_{CNT})J_0(Q\,R_i^{\perp})\Big/Q\,, \tag{A.21}$$

where $R_i^{\perp}$ is the modulus of the projection of $\langle R_i\rangle$ onto the plane perpendicular to the tube axis. Now the interference term for a SWCNT amounts to

$$I_{DC}(Q) = 8\pi^2 C_{1D}\, a_d\,\rho_A\, j_0(Qd_{D_2})\, e^{-\frac{1}{6}Q^2\left(u_{1D}^2+u_c^2\right)}R_{CNT}\,J_0(QR_{CNT})\,\frac{1}{N_cQ}\sum_i J_0(QR_i^{\perp})\,, \tag{A.22}$$

where i runs from 1 to N_c, being N_c the number of D_2 molecules of a unit cell of the corresponding 1D crystal.

For a distribution of MWCNTs of well-defined internal radius r_i and m layers separated by a distance h, the term $R_{CNT}\,J_0(QR_{CNT})$ transforms into

$$\sum_{n=1}^{m-1}(r_i+h(n-1))J_0(Q(r_i+h(n-1)))\,. \tag{A.23}$$

In our case the m distribution is not narrow, but those of r_i and h must be quite. Assuming r_i fixed, the average over the ensemble of MWCNTs modulates the terms in the sum over layers so that they are scaled down as n increases, since the statistics of larger n decreases because the instances of large m also decreases. Furthermore, for n small there are almost as many cases as for $n = 1$, that is, the histogram of n must start horizontally. A half-Gaussian decay of the n terms matches such specification and emerges as a natural choice. Altogether it yields

$$I_{DC}(Q) = 8\pi^2 C_{1D}\, a_d\,\rho_A\, j_0(Qd_{D_2})\, e^{-\frac{1}{3}Q^2u_{\text{eff}}^2}\frac{1}{N_cQ}\sum_i J_0(QR_i^{\perp})\sum_{n=1}^{\infty}\exp\left[-\frac{h^2(n-1)^2}{2\sigma_n^2}\right](r_i+h(n-1))J_0(Q(r_i+h(n-1)))\,, \tag{A.24}$$

where we have defined an effective rms displacement, u_{eff}, and σ_n is the dispersion of the half-Gaussian decay. In practical terms a value of 50 layers worked well for σ_n, for which a termination of the n sum at 250 were enough to reach convergence in a short cpu time. In general, there are far more sources of disorder than just the thermal fluctuations around the COMs. For instance, in the real MWCNTs h presents also dispersion with some systematic evolution with the number of layers [51]. All of these effects are here boldly represented through u_{eff}, chosen as the minimum needed to

maintain the line shape of the main ND peak (1.2 Å for the 62 hPa load and 1.5 Å for the 175 hPa case). The parameter h controls the location in Q of the dispersive profile. A value of 3.41 Å was consistent with both the ND measurements and the values reported in the literature [51]. Finally, the areal density of any nanotube is given by $\rho_A = 4/(3\sqrt{3}\ d_{cc}^2)$, where d_{cc} is the distance of the C – C bond in graphene taken here as 1.42 Å.

Appendix B. Materials and Methods

Appendix B.1 Experimental design

As for the confining system, we rely on samples of multi-walled carbon nanotubes (MWCNTs). For our interests, they present several advantages compared to single-walled nanotubes. To begin with, they are far stiffer. Given the weakness of the dispersive interactions among the molecules, tube bending should be avoided as much as possible to facilitate unperturbed crystallization. Besides, since the external diameters show a large dispersion in a typical MWCNT sample, they do not form so tightly and well ordered ropes, as their single-walled counterparts tend to do [52]. On the other hand, the interstitial sizes are typically much larger than those of the smaller inner diameters because the distribution of external diameters is centered at much higher values than those of the inner diameters (much larger also that the typical mean diameter of good quality SWCNTs samples). In such a case, it can be expected that the adsorption inside the smaller of the multi-walled tubes will not compete appreciably with 1D-like adsorption in the interstitials or external grooves of the ropes.

To select the smaller inner diameters as our confining systems we rely in the physics of adsorption. The smaller open inner diameter tubes produce the stronger attractive potential wells for the molecules so that they are filled first. For sufficiently small loads these micropores dominate the distribution of adsorbed molecules.

As for the probe to study the system, neutrons are uncharged, so that they can penetrate deeply into the target. Thus, they can explore the structure and dynamics of atomic and molecular arrangements buried into nanostructured materials, while at the same time making possible the use of complex sample environments such as cryogenic and gas handling equipment. Contrary to X-rays, they strongly interact with hydrogen. Since we are interested in structural information, we resort to the deuterium isotope in order to avoid the very large incoherent scattering of molecular hydrogen that does not contribute to the diffraction signal. Incoherent scattering stems from the random distribution of nuclear spin states along the sample, and implies the interchange of the spin state between the incident neutron and the nuclei. It can also be avoided in H_2 if prepared in its fundamental para-state, that only scatters coherently. However, the neutron energy must be well below 14.7 meV in order not to excite the molecular rotational levels responsible for the very strong incoherent scattering. This would limit the range of the scattering vector norm Q below 4 $Å^{-1}$, too short to properly explore the spatial scales involved.

Regarding the measurement protocol, we started by measuring the diffraction of the nanotubes sample (2 g) during a slow cooling/heating cycle (0.1 K decrement/increment each 70 s) between ≈ 24.5 K and 2 K while neutron diffraction signal was acquired in runs of 350 s. Then we proceeded by injecting very small quantities of D_2 into the sample can at 20 K until we observed a barely discernible liquid state diffraction signal. The equilibrium pressure at that point was 62 hPa. After heating at ≈ 24.5 K, the same cooling/heating cycle as before was done. The same thermal protocol was repeated increasing the D_2 load in each cycle up to a total of four loads, namely, 62 hPa, 175 hPa, 225 hPa, 284 hPa. Before the 175 hPa thermal cycle, in order to improve the statistics of the measurements at 62 hPa, a second cooling ramp was performed down to 2 K where neutron diffraction was measured in runs of 600 s up to a total of 31 runs. The cooling/heating rate during the thermal cycles was chosen as slow as it was feasible in order to remain as near as possible to thermodynamic equilibrium, corresponding in this case to those of saturated vapor pressure (SVP). From the adsorption isotherm in Fig. 2 it is clear that the four loads are far from the bulk condition at 20 K.

Appendix B.2 Multi-walled carbon nanotubes synthesis and treatment

The raw MWCNTs were prepared by the evaporation of pure graphite anodes in an electric arc discharge under a helium atmosphere of 66 kPa applying a current of 60 A and a voltage of 25 V [53]. The raw material was oxidized by heating to 973 K in open air during 30 min. After an annealing at 1223 K in Ar atmosphere during 10 h, around 2 g of the open MWCNT sample was obtained.

Appendix B.3 Deuterium

The deuterium gas was taken directly from a 95 L bottle of Air Liquide N30 Deuterium (purity ≥ 99.9 %; ∼ 10 ppm of D_2O and O_2 and ∼ 25 ppm of N_2).

Appendix B.4 Electron microscopy

The structure of the obtained MWCNT material was explored by TEM at the National Center for Electron Microscopy (CNME) in Madrid, Spain. Drops taken from a dispersion of the samples in ethanol were deposited over copper grids with holey carbon support films. Transmission electron micrographs were taken with a JEOL JEM2100 HT microscope operating at 200 kV.

Appendix B.5 Adsorption isotherm

The D_2 adsorption of the MWCNT sample was characterized by a measurement of the adsorbed moles as a function of the pressure at constant temperature (adsorption isotherm) using a standard volumetric procedure [29]. The chosen temperature was 20 K (D_2 triple point at 18.73 K). In essence, given a known volume, the adsorbed moles are obtained from the decrease in pressure they cause with respect to the same volume with no adsorbant. A homemade gas handling manifold was built to accurately manage the gas dosage. A layout of the system is shown in Fig. S1. All pipes and connections in the manifold are made of steel and Swagelok valves were used to connect the different volumes in the system. The pressure was determined with a Baratron® MKS 690 A absolute manometer with a full range scale of 1000 Torr and an accuracy of 0.12% of the reading. The reference volume V_R is provided by a calibrated steel vessel of volume 1045.7±2.3 cm^3. The MWCNT sample was located in an aluminium cylindrical can of 15 mm of inner diameter and 56 mm of height. The can was connected vertically to a specially built insertion stick (used to introduce the sample can in the cryostat) with an inner capillary for the D_2 injection. The stick was designed to match the standard ILL "Orange" cryostat [54,55]. This is the same kind of vertical cryostat used in the neutron scattering experiment. The inner capillary of the stick was connected through a valve to the end of the manifold labeled as "sample" in Fig. S1. Using the known value of V_R all the needed volumes are determined by expansion of He loads. In particular, the volume comprising from "sample" valve (closed) down to the sample can (not shown in the Figure) was 20.64±0.15 cm^3. Once the system volumes were determined, 0.521 g of the MWCNT

sample were loaded in the sample can, the sample stick was introduced in the cryostat and the temperature set to 20 K. From repeated D_2 loads in V_{inj} and subsequent expansions, the adsorbed moles were determined [29]. The sample temperature during the adsorption/desorption isotherm was $T = \langle T_S^i \rangle = 20.23 \pm 0.03$ K.

Appendix B.6 Neutron scattering experimental setup

The neutron scattering instrument of choice was D20 at the ILL in Grenoble, a reactor-based neutron facility (continuous neutron beam). The most characteristic feature of D20 is its very high neutron flux, which allows for real-time studies of many processes. The setup was chosen to maximize the neutron flux corresponding to a neutron wavelength of 1.30 Å. D20 is a powder diffractometer with a circular detection zone 1.47 m of radius, 4 m long and 15 cm high with the sample holder at the center of the circle (see Ref. [56] for details about D20). For the setup chosen the resolution remains below 0.02 $Å^{-1}$ until $Q = 5.5$ $Å^{-1}$, reaching 0.1 $Å^{-1}$ at $Q = 9$ $Å^{-1}$. Such resolution values are high enough to avoid resolution integrals in the data treatment. The gas handling manifold, described in Fig. S2, was located outside the neutron beam safety zone connected to the cryostat insertion stick through a 5-m-long 1-mm-diameter steel capillary. The injection volume, V_{inj}, used during the 20 K loads remained open during the neutron scattering measurements as a safety expansion volume. The sample can was a standard sample holder for the D20 instrument, namely, a 0.1 mm thick vanadium cylinder of 60 mm high and 8 mm of inner diameter. The neutron beam size was 8 mm width and 4 cm high. It was centered at the axis of the vanadium cylinder and the lower vertically edge of the beam located at the bottom part of the vanadium can. All the neutron irradiated volume was filled with MWCNTs sample (2 g). The pressure was monitored with a MKS 640 A manometer (1000 Torr range) and a MKS 627B manometer (15,000 Torr range). Since V_{inj} was open, the moles of D_2 irradiated by the neutron beam increased by a factor of around 1.4 from the equilibrium after load at 20 K to zero pressure solid at 2 K.

Appendix B.7 Neutron scattering data reduction

The raw data were corrected from detector efficiency and transformed to scattering vector reciprocal units using the LAMP software package freely available at the ILL facility [57,58]. Self-shielding and neutron absorption correction were estimated using the DAVE software package [59,60]. As expected, given the small D_2 quantities and the cylindrical geometry of the sample can, self-shielding and neutron absorption amounts to a small and essentially Q-independent correction. Likewise, multiple scattering corrections are again Q-independent [61]. Both can be ignored for our purposes, which do not depend on absolute scattering values. An important point to take into the account is the variation in the number of scatterers irradiated by the beam. During a thermal cycle, due to the varying thermodynamic conditions (thermal expansion/contraction, D_2 condensation and diffusion, etc), some grains of the MWCNT powder move in and out the irradiated volume. In absolute terms the effect is small but not negligible with respect to the smaller D_2 loads. To compensate the effect the $I(Q)$s of each run are divided by their corresponding total neutron count, which is proportional to the number of scatterers. In order to improve the statistics, all the runs corresponding to the pristine MWCNTs were added together, while for the low temperature $I(Q)$s of the loaded MWCNTs, only those below 11.5 K (well below solidification temperature) were considered.

With respect to the subtraction of the MWCNT signal, since self-shielding and neutron absorption can be considered Q-independent, $I_C(Q)$ is just given by an attenuation transmission factor applied to the $I(Q)$ corresponding to the empty MWCNTs. The porous nature of the D_2 distribution within the MWCNT sample does not allow for a theoretical calculation of the effective transmissions. Instead, we have just heuristically adjusted the corresponding values, namely, 0.994 at 62 hPa, 0.9675 at 175 hPa, 0.940 at 225 hPa and 0.930 at 284 hPa.

Appendix B.8 Numerical methods. Molecular Dynamics

Molecular Dynamics (MD) simulations used in our nonlinear fitting analysis have been carried out using Large-scale Atomic/Molecular Massively Parallel Simulator (LAMMPS) code [62]. Taking into account the quantum delocalization of the nuclear rotational degrees of freedom we have considered for the D_2–D_2 interaction an isotropic effective potential [12] adapted to the LAMMPS code. For the C – C interaction we have relied in the Adaptive Intermolecular Reactive Empirical Bond Order (AIREBO) potential described in Ref. [63] as it is included in the LAMMPS package. In the case of the D_2–C interaction, we have relied in the anisotropic pair potential developed in Ref. [25] out of accurate *ab initio* calculations using Density Functional Theory (DFT) based on Symmetry Adapted Perturbation Theory (SAPT(DFT)), again adapted to LAMMPS. For details, including the parameterization used, see Supplementary Material in Ref. [25]. Thermalization has been achieved through the Berendsen thermostat [64], which presents a large thermal stability suitable for small samples. The chosen time step is one fs. The specifics of the procedure in the present calculations are given in the Supplementary Information.

Appendix B.9 Numerical methods. DFT

For the DFT calculations we have relied on the Perdew, Burke, and Ernzerhof (PBE) approach [65] as implemented in the CASTEP code [66]. The pseudopotentials are those corresponding to the 00PBE_OP.recpot family as given by the Materials Studio package. The dispersive interactions are treated using the semi-empirical dispersion correction scheme (DFT-SEDC) [67] with Tkatchenko and Scheffler (TS) correction [68] (hydrogen atoms corrected to deuterium mass). The energy cutoff of the plane wave basis set was 900 eV, only one k point was used and the maximum force tolerance per atom was set to 0.006 eV/Å. The CNT containing the D_2 molecules is a (10,5) SWCNT with a length of 22.6211727 Å and 280 carbon atoms. The specifics of the procedure are given in the Supplementary Material and in Table SIII therein.

References

[1] P.M. Ajayan, S. Iijima, Capillarity-induced filling of carbon nanotubes, Nature 361 (6410) (1993) 333–334, https://doi.org/10.1038/361333a0.
[2] R.R. Meyer, J. Sloan, R.E. Dunin-Borkowski, A.I. Kirkland, M.C. Novotny, S.R. Bailey, J.L. Hutchison, M.L. Green, Discrete atom imaging of one-dimensional crystals formed within single-walled carbon nanotubes, Science 289 (5483) (2000) 1324–1326, https://doi.org/10.1126/science.289.5483.1324.
[3] M. Monthioux, Carbon Meta-Nanotubes: Synthesis, Properties and Applications, John Wiley & Sons, 2011.
[4] C.E. Giusca, V. Stolojan, J. Sloan, F. Börrnert, H. Shiozawa, K. Sader, M.H. Rümmeli, B. Büchner, S.R.P. Silva, Confined crystals of the smallest phase-change material, Nano Lett. 13 (9) (2013) 4020–4027, https://doi.org/10.1021/nl4010354.
[5] A.A. Eliseev, N.S. Falaleev, N.I. Verbitskiy, A.A. Volykhov, L.V. Yashina, A.S. Kumskov, V.G. Zhigalina, A.L. Vasiliev, A.V. Lukashin, J. Sloan, et al., Size-dependent structure relations between nanotubes and encapsulated nanocrystals, Nano Lett. 17 (2) (2017) 805–810, https://doi.org/10.1021/acs.nanolett.6b04031.
[6] K. Koga, G. Gao, H. Tanaka, X.C. Zeng, Formation of ordered ice nanotubes inside carbon nanotubes, Nature 412 (6849) (2001) 802, https://doi.org/10.1038/35090532.
[7] A.I. Kolesnikov, J.-M. Zanotti, C.-K. Loong, P. Thiyagarajan, A.P. Moravsky,

R.O. Loutfy, C.J. Burnham, Anomalously soft dynamics of water in a nanotube: a revelation of nanoscale confinement, Phys. Rev. Lett. 93 (3) (2004), 035503, https://doi.org/10.1103/physrevlett.93.035503.
[8] Y. Maniwa, H. Kataura, M. Abe, A. Udaka, S. Suzuki, Y. Achiba, H. Kira, K. Matsuda, H. Kadowaki, Y. Okabe, Ordered water inside carbon nanotubes: formation of pentagonal to octagonal ice-nanotubes, Chem. Phys. Lett. 401 (4–6) (2005) 534–538, https://doi.org/10.1016/j.cplett.2004.11.112.
[9] F.J. Bermejo, K. Kinugawa, C. Cabrillo, S.M. Bennington, B. Fåk, M.T. Fernández-Díaz, P. Verkerk, J. Dawidowski, R. Fernández-Perea, Quantum effects on liquid dynamics as evidenced by the presence of well-defined collective excitations in liquidpara-hydrogen, Phys. Rev. Lett. 84 (23) (2000) 5359–5362, https://doi.org/10.1103/physrevlett.84.5359.
[10] F. Fernandez-Alonso, C. Cabrillo, R. Fernández-Perea, F.J. Bermejo, M.A. González, C. Mondelli, E. Farhi, Solid para-hydrogen as the paradigmatic quantum crystal: three observables probed by ultrahigh-resolution neutron spectroscopy, Phys. Rev. B 86 (14) (2012) 144524, https://doi.org/10.1103/physrevb.86.144524.
[11] C. Cabrillo, F. Fernández-Alonso, R. Fernández-Perea, F.J. Bermejo, M.A. González, C. Mondelli, E. Farhi, Crystallization of para-Hydrogen: a quantum phase transition at finite temperature? J. Phys. Conf. 663 (2015), 012006 https://doi.org/10.1088/1742-6596/663/1/012006.
[12] I.F. Silvera, The solid molecular hydrogens in the condensed phase: fundamentals and static properties, Rev. Mod. Phys. 52 (2) (1980) 393–452, https://doi.org/10.1103/revmodphys.52.393.
[13] L. Mattera, F. Rosatelli, C. Salvo, F. Tommasini, U. Valbusa, G. Vidali, Selective adsorption of $^1H_2$ and $^2H_2$ on the (0001) graphite surface, Surf. Sci. 93 (2–3) (1980) 515–525, https://doi.org/10.1016/0039-6028(80)90279-4.
[14] Y. Ma, Y. Xia, M. Zhao, M. Ying, Structures of hydrogen molecules in single-walled carbon nanotubes, Chem. Phys. Lett. 357 (1–2) (2002) 97–102, https://doi.org/10.1016/S0009-2614(02)00448-7.
[15] Y. Xia, M. Zhao, Y. Ma, X. Liu, M. Ying, L. Mei, Condensation and phase transition of hydrogen molecules confined in single-walled carbon nanotubes, Phys. Rev. B 67 (11) (2003) 115117, https://doi.org/10.1103/physrevb.67.115117.
[16] M. Ying, Y. Xia, X. Liu, F. Li, B. Huang, Z. Tan, Quasi-one-dimensional liquid hydrogen confined in single-walled carbon nanotubes, Appl. Phys. A 78 (5) (2004) 771–775.
[17] X. Fan, E. Dickey, P. Eklund, K. Williams, L. Grigorian, R. Buczko, S. Pantelides, S. Pennycook, Atomic arrangement of iodine atoms inside single-walled carbon nanotubes, Phys. Rev. Lett. 84 (20) (2000) 4621.
[18] L. Guan, K. Suenaga, Z. Shi, Z. Gu, S. Iijima, Polymorphic structures of iodine and their phase transition in confined nanospace, Nano Lett. 7 (6) (2007) 1532–1535.
[19] D. Rybkovskiy, A. Impellizzeri, E. Obraztsova, C. Ewels, Polyiodide structures in thin single-walled carbon nanotubes: a large-scale density-functional study, Carbon 142 (2019) 123–130, https://doi.org/10.1016/j.carbon.2018.10.049.
[20] M.C. Gordillo, J. Boronat, J. Casulleras, Zero-temperature equation of state of quasi-one-dimensional H_2, Phys. Rev. Lett. 85 (11) (2000) 2348–2351, https://doi.org/10.1103/physrevlett.85.2348.
[21] M. Boninsegni, Ground state phase diagram of parahydrogen in one dimension, Phys. Rev. Lett. 111 (23) (2013) 235303, https://doi.org/10.1103/physrevlett.111.235303.
[22] M. Rossi, F. Ancilotto, Superfluid behavior of quasi-one-dimensional p-H_2 inside a carbon nanotube, Phys. Rev. B 94 (10) (2016) 100502, https://doi.org/10.1103/physrevb.94.100502.
[23] A.D. Maestro, M. Boninsegni, Absence of superfluidity in a quasi-one-dimensional para-hydrogen fluid adsorbed inside carbon nanotubes, Phys. Rev. B 95 (5) (2017), 054517, https://doi.org/10.1103/physrevb.95.054517.
[24] G. Ferré, M.C. Gordillo, J. Boronat, Luttinger parameter of quasi-one-dimensional para-H_2, Phys. Rev. B 95 (6) (2017) 64502, https://doi.org/10.1103/physrevb.95.064502.
[25] M.P. de Lara-Castells, A.W. Hauser, A.O. Mitrushchenkov, R. Fernández-Perea, Quantum confinement of molecular deuterium clusters in carbon nanotubes: ab initio evidence for hexagonal close packing, Phys. Chem. Chem. Phys. 19 (42) (2017) 28621–28629, https://doi.org/10.1039/c7cp05869a.
[26] M. Muris, M. Bienfait, P. Zeppenfeld, N. Dupont-Pavlovsky, M. Johnson, O. Vilches, T. Wilson, Diffraction study of CD 4 and d 2 adsorbed on carbon nanotubes, Appl. Phys. Mater. Sci. Process 74 (2002) s1293–s1295, https://doi.org/10.1007/s003390101220, 0.
[27] M. Bienfait, P. Zeppenfeld, N. Dupont-Pavlovsky, M. Muris, M.R. Johnson, T. Wilson, M. DePies, O.E. Vilches, Thermodynamics and structure of hydrogen, methane, argon, oxygen, and carbon dioxide adsorbed on single-wall carbon nanotube bundles, Phys. Rev. B 70 (3) (2004) 35410, https://doi.org/10.1103/physrevb.70.035410.
[28] N. Floquet, J. Coulomb, G. André, Hydrogen sorption in MCM-41 by neutron diffraction study. Characterization of the porous structure of MCM-41 and the growth mode of the hydrogen confined phases, Microporous Mesoporous Mater. 72 (1–3) (2004) 143–152, https://doi.org/10.1016/j.micromeso.2004.04.014.
[29] F. Rouquerol, J. Rouquerol, K. Sing, Adsorption by Powders and Porous Solids, Acad. Press, San Diego, Calif. [u.a.], 1999.
[30] E.W. Lemmon, M.O. McLinden, D.G. Friend, NIST Standard Reference Database Number, vol. 69, National Institute of Standards and Technology, Gaithersburg, MD, 2005. Ch. Thermophysical Properties of Fluid Systems.
[31] V.F. Sears, Theory of cold neutron scattering by homonuclear diatomic liquids: I. free rotation, Can. J. Phys. 44 (6) (1966) 1279–1297, https://doi.org/10.1139/p66-108.
[32] L.D. Gelb, K.E. Gubbins, R. Radhakrishnan, M. Sliwinska-Bartkowiak, Phase separation in confined systems, Rep. Prog. Phys. 62 (12) (1999) 1573–1659, https://doi.org/10.1088/0034-4885/62/12/201.
[33] C.S. Barrett, L. Meyer, J. Wasserman, Crystal structure of solid hydrogen and deuterium, and of neon—hydrogen and neon—deuterium mixtures, J. Chem. Phys. 45 (3) (1966) 834–837, https://doi.org/10.1063/1.1727691.
[34] A.F. Schuch, R.L. Mills, Crystal structure of deuterium at low temperatures, Phys. Rev. Lett. 16 (14) (1966) 616–618, https://doi.org/10.1103/physrevlett.16.616.
[35] R.O. Erickson, Tubular packing of spheres in biological fine structure, Science 181 (4101) (1973) 705–716, https://doi.org/10.1126/science.181.4101.705.
[36] C. Lu, Y. Cheng, Q. Pan, X. Tao, B. Yang, G. Ye, One-dimensional growth of zinc crystals on a liquid surface, Sci. Rep. 6 (1) (2016) 19870, https://doi.org/10.1038/srep19870.
[37] Y. Cheng, C. Lu, B. Yang, X. Tao, J. Wang, G. Ye, One-dimensional crystal growth model on a square lattice substrate, Phys. Lett. 380 (37) (2016) 2989–2992, https://doi.org/10.1016/j.physleta.2016.07.023.
[38] A. Frei, E. Gutsmiedl, C. Morkel, A.R. Müller, S. Paul, M. Urban, H. Schober, S. Rols, T. Unruh, M. Hölzel, Density of states in solid deuterium: inelastic neutron scattering study, Phys. Rev. B 80 (6) (2009), 064301, https://doi.org/10.1103/physrevb.80.064301.
[39] The locus of absorption minima is obtained from the Berthelot rule applied to the corresponding Lennard-Jones potentials.
[40] K. Edgar, S.C. Hendy, D. Schebarchov, R.D. Tilley, Reverse capillary action in carbon nanotubes: sucking metal nanoparticles out of nanotubes, Small 7 (6) (2011) 737–740, https://doi.org/10.1002/smll.201001857.
[41] J. Yun, W. Jeon, F.A. Khan, J. Lee, S. Baik, Reverse capillary flow of condensed water through aligned multiwalled carbon nanotubes, Nanotechnology 26 (23) (2015) 235701, https://doi.org/10.1088/0957-4484/26/23/235701.
[42] S. Gravelle, C. Ybert, L. Bocquet, L. Joly, Anomalous capillary filling and wettability reversal in nanochannels, Phys. Rev. 93 (3) (2016), 033123, https://doi.org/10.1103/physreve.93.033123.
[43] T. Ohba, Limited quantum helium transportation through nano-channels by quantum fluctuation, Sci. Rep. 6 (1) (2016) 28992, https://doi.org/10.1038/srep28992.
[44] A.W. Hauser, M.P. de Lara-Castells, Carbon nanotubes immersed in superfluid helium: the impact of quantum confinement on wetting and capillary action, J. Phys. Chem. Lett. 7 (23) (2016) 4929–4935, https://doi.org/10.1021/acs.jpclett.6b02414.
[45] A.W. Hauser, A.O. Mitrushchenkov, M.P. de Lara-Castells, Quantum nuclear motion of helium and molecular nitrogen clusters in carbon nanotubes, J. Phys. Chem. C 121 (7) (2017) 3807–3821, https://doi.org/10.1021/acs.jpcc.6b12959.
[46] T. E. Markland, M. Ceriotti, Nuclear quantum effects enter the mainstream, Nature Reviews Chemistry 2 (3). doi:10.1038/s41570-017-0109.
[47] G.L. Squires, Introduction to the Theory of Thermal Neutron Scattering, Dover Publications, 1997.
[48] G. Placzek, The scattering of neutrons by systems of heavy nuclei, Phys. Rev. 86 (3) (1952) 377–388, https://doi.org/10.1103/physrev.86.377.
[49] S.W. Lovesey, The Theory of Neutron Scattering from Condensed Matter, vol. I, Oxford University Press, 1986.
[50] W. Langel, D.L. Price, R.O. Simmons, P.E. Sokol, Inelastic neutron scattering from liquid and solid hydrogen at high momentum transfer, Phys. Rev. B 38 (16) (1988) 11275–11283, https://doi.org/10.1103/physrevb.38.11275.
[51] O.V. Kharissova, B.I. Kharisov, Variations of interlayer spacing in carbon nanotubes, RSC Adv. 4 (58) (2014) 30807–30815, https://doi.org/10.1039/c4ra04201h.
[52] A. Thess, R. Lee, P. Nikolaev, H. Dai, P. Petit, J. Robert, C. Xu, Y.H. Lee, S.G. Kim, A.G. Rinzler, D.T. Colbert, G.E. Scuseria, D. Tomanek, J.E. Fischer, R.E. Smalley, Crystalline ropes of metallic carbon nanotubes, Science 273 (5274) (1996) 483–487, https://doi.org/10.1126/science.273.5274.483.
[53] A. Benito, W. Maser, M. Martinez, Carbon nanotubes: from production to functional composites, Int. J. Nanotechnol. 2 (1/2) (2005) 71, https://doi.org/10.1504/ijnt.2005.006975.
[54] D. Brochier, Cryostat à température variable pour mesures neutroniques ou optiques, Tech. Rep. 77/74 (1977). Institut Laue-Langevin.
[55] Orange cryostats information, accessed October 2020. URL, https://www.ill.eu/users/support-labs-infrastructure/sample-environment/equipment/low-temperature/orange-cryogen-free-cryostats/.
[56] D20 instrument information, accessed October, 2020. URL, https://www.ill.eu/users/instruments/instruments-list/d20/description/instrument-layout/.
[57] D. Richard, M. Ferrand, G.J. Kearley, Analysis and visualisation of neutron-scattering data, J. Neutron Res. 4 (1) (1996) 33–39, https://doi.org/10.1080/10238169608200065.
[58] LAMP package information, accessed October, 2020. URL, https://www.ill.eu/users/support-labs-infrastructure/software-scientific-tools/lamp/.
[59] R.T. Azuah, L.R. Kneller, Y. Qiu, P.L.W. Tregenna-Piggott, C.M. Brown, J.R.D. Copley, R.M. Dimeo, DAVE: a comprehensive software suite for the reduction, visualization, and analysis of low energy neutron spectroscopic data, Journal of Research of the National Institute of Standards and Technology 114 (6) (2009) 341, https://doi.org/10.6028/jres.114.025.
[60] DAVE package information, accessed September, 2020. URL, https://www.ncnr.nist.gov/dave/index.html.

[61] R. Zorn, Multiple scattering correction of polarized neutron diffraction data, Nucl. Instrum. Methods Phys. Res. 479 (2002) 568–584, https://doi.org/10.1016/S0168-9002(01)00903-2.
[62] S. Plimpton, Fast parallel algorithms for short-range molecular dynamics, J. Comput. Phys. 117 (1) (1995) 1–19, https://doi.org/10.1006/jcph.1995.1039.
[63] S.J. Stuart, A.B. Tutein, J.A. Harrison, A reactive potential for hydrocarbons with intermolecular interactions, J. Chem. Phys. 112 (14) (2000) 6472–6486, https://doi.org/10.1063/1.481208.
[64] H.J.C. Berendsen, J.P.M. Postma, W.F. van Gunsteren, A. DiNola, J.R. Haak, Molecular dynamics with coupling to an external bath, J. Chem. Phys. 81 (8) (1984) 3684–3690, https://doi.org/10.1063/1.448118.
[65] J.P. Perdew, K. Burke, M. Ernzerhof, Generalized gradient approximation made simple, Phys. Rev. Lett. 77 (1996) 3865–3868, https://doi.org/10.1103/PhysRevLett.77.3865.
[66] S.J. Clark, M.D. Segall, C.J. Pickard, P.J. Hasnip, M.J. Probert, K. Refson, M. Payne, First principles methods using CASTEP, Z. für Kristallogr. - Cryst. Mater. 220 (2005) 567–570, https://doi.org/10.1524/zkri.220.5.567.65075.
[67] E.R. McNellis, J. Meyer, K. Reuter, Azobenzene at coinage metal surfaces: role of dispersive van der waals interactions, Phys. Rev. B 80 (20) (2009) 205414, https://doi.org/10.1103/physrevb.80.205414.
[68] A. Tkatchenko, M. Scheffler, Accurate molecular van der waals interactions from ground-state electron density and free-atom reference data, Phys. Rev. Lett. 102 (2009), 073005, https://doi.org/10.1103/PhysRevLett.102.073005.